Numerical experiments of fracture-induced velocity and attenuation anisotropy

J. M. Carcione,[1] S. Picotti[1] and J. E. Santos[2,3,4]

[1]*Istituto Nazionale di Oceanografia e di Geofisica Sperimentale (OGS), Borgo Grotta Gigante 42c, 34010 Sgonico, Trieste, Italy. E-mail: jcarcione@inogs.it*
[2]*CONICET, Instituto del Gas y del Petróleo, Facultad de Ingeniera, Universidad de Buenos Aires, Av. Las Heras 2214 Piso 3 C1127AAR Buenos Aires, Argentina*
[3]*Universidad Nacional de La Plata, La Plata, Argentina*
[4]*Department of Mathematics, Purdue University, 150 N. University Street, West Lafayette, Indiana 47907-2067, USA*

SUMMARY

Fractures are common in the Earth's crust due to different factors, for instance, tectonic stresses and natural or artificial hydraulic fracturing caused by a pressurized fluid. A dense set of fractures behaves as an effective long-wavelength anisotropic medium, leading to azimuthally varying velocity and attenuation of seismic waves. Effective in this case means that the predominant wavelength is much longer than the fracture spacing. Here, fractures are represented by surface discontinuities in the displacement $\mathbf{u}$ and particle velocity $\mathbf{v}$ as $[\kappa \cdot \mathbf{u} + \eta \cdot \mathbf{v}]$, where the brackets denote the discontinuity across the surface, κ is a fracture stiffness and η is a fracture viscosity.

We consider an isotropic background medium, where a set of fractures are embedded. There exists an analytical solution—with five stiffness components—for equispaced plane fractures and an homogeneous background medium. The theory predicts that the equivalent medium is transversely isotropic and viscoelastic. We then perform harmonic numerical experiments to compute the stiffness components as a function of frequency, by using a Galerkin finite-element procedure, and obtain the complex velocities of the medium as a function of frequency and propagation direction, which provide the phase velocities, energy velocities (wavefronts) and quality factors. The algorithm is tested with the analytical solution and then used to obtain the stiffness components for general heterogeneous cases, where fractal variations of the fracture compliances and background stiffnesses are considered.

Key words: Numerical solutions; Seismic anisotropy; Seismic attenuation; Wave propagation; Fractures and faults.

1 INTRODUCTION

Seismic wave propagation through fractures and cracks is an important subject in exploration and production geophysics, earthquake seismology and mining (Steen *et al.* 1998; Nelson 2001). Fractures constitute the sources of earthquakes (Daub & Carlson 2010) and hydrocarbon and geothermal reservoirs are mainly composed of fractured rocks (Xu & Pruess 2001). This makes characterizing the seismic properties of fractures essential in those fields of research. For instance, aligned vertical fractures can lead to an azimuthal anisotropy (Schoenberg *et al.* 1999; Gray & Head 2000), particularly azimuthal dependence of velocity and attenuation, which is sensitive to key properties of the reservoir, such as fluid type, flow direction, porosity, permeability, etc.

Seismic anisotropy and attenuation are frequency dependent. Carcione (1992) obtained the first model for Q-anisotropy based on Backus averaging (see Carcione 2007). This model has been further studied by Picotti *et al.* (2010, 2012), who have shown how to compute the stiffness components of the effective transversely isotropic and viscoelastic (TIV) medium with quasi-static numerical experiments. These models are based on viscoelastic layers and do not consider fractures explicitly.

Modelling fractures requires a suitable interface model. Schoenberg (1980, 1983) proposes the so-called linear-slip model, based on the discontinuity of the displacement across the interface (Schoenberg's model). A generalization (Carcione 1996) states that the stress components are proportional to the displacement and velocity discontinuities through the specific stiffnesses and specific viscosities, respectively. Displacement discontinuities conserve energy and yield frequency-dependent reflection and transmission coefficients, while velocity discontinuities generate energy loss at the interface. The specific viscosity accounts for the presence of a liquid. Chichinina *et al.* (2009) and Carcione *et al.* (2012) obtained analytical solutions for the TIV and more general anisotropic cases, respectively, i.e. the complex and frequency-dependent stiffness components.

Schoenberg's model, generalized to the viscoelastic case, has been introduced into the wave equation and solved numerically by Carcione (1996, 2007). He used pseudo-spectral methods and domain decomposition (two grids) to model wave propagation and attenuation through a fracture. Carcione (1998) generalized the method to the anisotropic case. Recently, Zhang (2005), Zhang & Gao (2009) and De Basabe *et al.* (2011) implemented Schoenberg's model (purely elastic) by using finite-volume and finite-element methods, respectively. All these schemes treat a single fracture as a non-welded interface that satisfies the linear-slip displacement-discontinuity conditions instead of using equivalent medium theories or layers as, for instance, in Coates & Schoenberg (1995).

Schoenberg's model for a dense set of fractures has never been simulated with a numerical method. In order to test the theory and develop a novel numerical solver that can be used in more general situations, e.g. when analytical solutions do no exist, we use a frequency-domain finite-element method (FEM) to determine the complex stiffness coefficients of the TIV equivalent medium. The methodology consists in applying time-harmonic oscillatory tests at a finite number of frequencies on a sample containing a dense set of viscoelastic fractures. It is based on the wave equation of motion, with the explicit introduction of the linear-slip boundary conditions into the FEM. Similar tests have been successfully performed for a dense set of layers (Picotti *et al.* 2010, 2012; Carcione *et al.* 2011; Santos *et al.* 2012).

2 THE INTERFACE (FRACTURE) MODEL

Let us consider a planar anelastic fracture. The boundary conditions at the interface are

$$\kappa \cdot [\mathbf{u}] + \eta \cdot [\mathbf{v}] = \sigma \cdot \mathbf{n}, \tag{1}$$

(Pyrak-Nolte *et al.* 1990; Carcione 1996), where $\mathbf{u}$ and $\mathbf{v}$ are the displacement and particle-velocity components, respectively, σ is the 3×3 stress tensor, $\mathbf{n}$ is the unit normal to the fracture, κ is the specific stiffness matrix, and η is the specific viscosity matrix (both of dimension 3×3). They have dimensions of stiffness and viscosity per unit length, respectively. Moreover, the symbol '·' indicates scalar product and the brackets denote discontinuities across the interface, such that for a field variable ϕ, it is $[\phi] = \phi_2 - \phi_1$, where 1 and 2 indicate the two sides of the fracture and $\mathbf{n}$ points from 2 to 1.

The particle velocity is given by $\mathbf{v} = \dot{\mathbf{u}}$, where a dot above a variable indicates time differentiation. In the Fourier domain, $\mathbf{v} = i\omega\mathbf{u}$, where ω is the angular frequency and $i = \sqrt{-1}$. Eq. (1) then becomes

$$[\mathbf{u}] = \mathbf{Z} \cdot (\sigma \cdot \mathbf{n}), \tag{2}$$

where

$$\mathbf{Z} = (\kappa + i\omega\eta)^{-1} \tag{3}$$

is a fracture compliance matrix, whose dimension is length/stress. This approach is equivalent to the linear-slip model introduced by Schoenberg (1980). In fact, eq. (3), with $\eta = 0$, is given in Coates & Schoenberg (1995). Three models have been studied by Liu *et al.* (2000) to obtain the expression of $\mathbf{Z}$ for different fracture models.

The compliance matrix $\mathbf{Z}$ of the set of fractures is diagonal with positive definite real and imaginary parts

$$\mathbf{Z} = \begin{pmatrix} Z_1 & 0 & 0 \\ 0 & Z_2 & 0 \\ 0 & 0 & Z_3 \end{pmatrix} = \begin{pmatrix} (\kappa_1 + i\omega\eta_1)^{-1} & 0 & 0 \\ 0 & (\kappa_2 + i\omega\eta_2)^{-1} & 0 \\ 0 & 0 & (\kappa_3 + i\omega\eta_3)^{-1} \end{pmatrix}, \tag{4}$$

where Z_1 is the normal compliance, Z_2 is the horizontal tangential compliance and Z_3 is the vertical tangential compliance. The fact that there are no off-diagonal components means that, across the fractures, the normal motion is uncoupled from the tangential motion.

A common situation in the Earth's crust is to have a set of parallel fractures. The mechanical representation of the fracture boundary condition is given by a Kelvin-Voigt model, according to the stress-displacement relation

$$\sigma \cdot \mathbf{n} = (\kappa + i\omega\eta) \cdot [\mathbf{u}]. \tag{5}$$

The quantity $\kappa + i\omega\eta$ is the complex modulus per unit length of the Kelvin-Voigt element (e.g. Carcione 2007).

A displacement discontinuity yields compliance, while a discontinuity in the particle velocity implies an energy loss at the interface (Carcione 1996, 1998, 2007); $\kappa = 0$ gives the particle-velocity discontinuity model and $\eta = 0$ gives the displacement discontinuity model. On the other hand, if $\kappa \to \infty$ or $\eta \to \infty$, the model gives a welded interface.

3 THE EQUIVALENT ANISOTROPIC MEDIUM. ANALYTICAL SOLUTION

We consider a set of horizontal and parallel fractures. Let us introduce

$$Z_N = \frac{Z_1}{L}, \quad Z_H = \frac{Z_2}{L}, \quad Z_V = \frac{Z_3}{L}, \tag{6}$$

where L is a characteristic length, such that these quantities have dimensions of compliance, and

$$\kappa_N = L\kappa_1, \quad \kappa_H = L\kappa_2, \quad \kappa_V = L\kappa_3,$$

$$\eta_N = L\eta_1, \quad \eta_H = L\eta_2, \quad \eta_V = L\eta_3, \tag{7}$$

have dimensions of stiffness and viscosity, respectively. The quantity L, called h in Grechka *et al.* (2003) (see their eq. 3), is the average fracture spacing, which has to be much smaller than the dominant wavelength of the pulse. Thus,

$$Z_N = \frac{1}{\kappa_N + i\omega\eta_N}, \quad Z_H = \frac{1}{\kappa_H + i\omega\eta_H}, \quad Z_V = \frac{1}{\kappa_V + i\omega\eta_V}. \tag{8}$$

If the background medium is isotropic, with elasticity components (Lamé constants) c_{12} and c_{55}, and the fracture set is rotationally invariant, we have $Z_H = Z_V \equiv Z_T$, and the equivalent medium is TIV with a vertical symmetry axis (VTIV), whose stiffness matrix is

$$\mathbf{P} = \begin{pmatrix} c_{11} - c_{12}^2 Z_N c_N & c_{12} - c_{12}^2 Z_N c_N & c_{12}c_N & 0 & 0 & 0 \\ c_{12} - c_{12}^2 Z_N c_N & c_{11} - c_{12}^2 Z_N c_N & c_{12}c_N & 0 & 0 & 0 \\ c_{12}c_N & c_{12}c_N & c_{11}c_N & 0 & 0 & 0 \\ 0 & 0 & 0 & c_{55}c_T & 0 & 0 \\ 0 & 0 & 0 & 0 & c_{55}c_T & 0 \\ 0 & 0 & 0 & 0 & 0 & c_{55} \end{pmatrix} \tag{9}$$

(Schoenberg 1983; Chichinina *et al.* 2009; Carcione *et al.* 2012), where $c_{11} = c_{12} + 2c_{55}$,

$$c_N = (1 + c_{11}Z_N)^{-1} \quad \text{and} \quad c_T = (1 + c_{55}Z_T)^{-1}. \tag{10}$$

The stiffness matrix in Coates & Schoenberg (1995) is equivalent to $\mathbf{P}$ of eq. (9) considering the lossless case ($\boldsymbol{\eta} = 0$). If $\boldsymbol{\eta} \neq 0$, eq. (9) is equivalent to the medium studied by Chichinina *et al.* (2009).

Eq. (9) represents an equivalent medium corresponding to a set of highly permeable fractures and it is obtained as a limit case of a layered medium, where one of the layers is very soft, thin and viscoelastic. In particular, the components p_{IJ} of matrix $\mathbf{P}$ are obtained by assuming a periodic medium composed of two layers, where one of the layers has the Lamé constants λ and μ (the background medium) and the other, representing the fracture, is very thin with Lamé constants $\mu_f = pL\beta = p/Z_T$ and $E_f = \lambda_f + 2\mu_f = pL\alpha = p/Z_N$, where $p \ll 1$ is the volume proportion of fractures, and L is the fracture spacing (constant). The displacement discontinuities (boundary conditions) associated with the fractures are $[u_3] = LZ_N\sigma_{33}$ and $[u_1] = LZ_T\sigma_{13}$ along the x_3- and x_1-directions, respectively (Schoenberg 1983, eqs 21–23; Carcione *et al.* 2012).

Denoting by e_{ij} and τ_{ij} the strain and stress tensors of the equivalent TIV medium at the macroscale, the stress–strain relations are

$$\tau_{11} = p_{11}e_{11} + p_{12}e_{22} + p_{13}e_{33},$$

$$\tau_{22} = p_{12}e_{11} + p_{11}e_{22} + p_{13}e_{33},$$

$$\tau_{33} = p_{13}e_{11} + p_{13}e_{22} + p_{33}e_{33},$$

$$\tau_{23} = 2p_{55}e_{23}, \tag{11}$$

$$\tau_{13} = 2p_{55}e_{13},$$

$$\tau_{12} = 2p_{66}e_{12},$$

where $p_{66} = (p_{11} - p_{12})/2$. In the next section we present a numerical procedure to determine the components p_{IJ} in (11) and the corresponding phase velocities and quality factors. These properties, which depend on frequency and propagation direction, are given in the Appendix. We show that for this purpose it is sufficient to perform a collection of oscillatory tests on representative 2-D samples of the material.

4 THE METHODOLOGY

Let $\mathbf{u}$, $\epsilon_{ij}(\mathbf{u})$ and $\sigma_{ij}(\mathbf{u})$ denote the frequency-domain displacement vector, strain components and stress components of the background medium. The stress–strain relations and equation of motion are

$$\sigma_{ij} = c_{12}\epsilon_{kk}\delta_{ij} + 2c_{55}\epsilon_{ij} \tag{12}$$

and

$$\rho\omega^2\mathbf{u}(x, z, \omega) + \nabla \cdot \boldsymbol{\sigma}(\mathbf{u}(x, z, \omega)) = 0, \tag{13}$$

(Ben-Menahem & Singh 1981), respectively, where implicit summation of repeated indices is assumed.

4.1 FE implementation

We consider a rectangular sample Ω and set the boundaries as $\Gamma = \Gamma^L \cup \Gamma^R \cup \Gamma^B \cup \Gamma^T$, where

$$\Gamma^L = \{(x, z) \in \Gamma : x = 0\}, \quad \Gamma^R = \{(x, z) \in \Gamma : x = \mathcal{L}\},$$

$$\Gamma^B = \{(x, z) \in \Gamma : z = 0\}, \quad \Gamma^T = \{(x, z) \in \Gamma : z = \mathcal{L}\}.$$

are the left (L), right (R), bottom (B), and top (T) boundaries of the sample, respectively. Denote by $\mathbf{n}$ the unit outer normal on Γ and let $\mathbf{m}$ be a unit tangent on Γ so that $\{\mathbf{n}, \mathbf{m}\}$ is an orthonormal system on Γ.

Let us assume that we have a set of $J^{(f)}$ horizontal fractures $\Gamma^{(f,l)}$, $l = 1, \cdots, J^{(f)}$ each one of length $\mathcal{L}$ in the domain Ω. This set of fractures divides the domain in a collection of non-overlapping rectangles $R^{(l)}$, $l = 1, \cdots, J^{(f)} + 1$, so that

$$\Omega = \cup_{l=1}^{J^{(f)}+1} R^{(l)}.$$

Consider a fracture $\Gamma^{(f,l)}$ and the two rectangles $R^{(l)}$ and $R^{(l+1)}$ having as a common side $\Gamma^{(f,l)}$. Let $\mathbf{n}_{l,l+1}$, $\mathbf{m}_{l,l+1}$ be the unit outer normal and a unit tangent (oriented counterclockwise) on $\Gamma^{(f,l)}$ from $R^{(l)}$ to $R^{(l+1)}$, such that $\{\mathbf{n}_{l,l+1}, \mathbf{m}_{l,l+1}\}$ is an orthonormal system on $\Gamma^{(f,l)}$.

The boundary conditions at fracture $\Gamma^{(f,l)}$ are given by eq. (5). More precisely, if $\mathbf{u}^{(l)} = \mathbf{u}|_{R^{(l)}}$ denotes the restriction of $\mathbf{u}$ to $R^{(l)}$, we impose

$$\boldsymbol{\sigma}(\mathbf{u}^{(l)})\mathbf{n}_{l,l+1} = \boldsymbol{\sigma}(\mathbf{u}^{(l+1)})\mathbf{n}_{l,l+1}, \quad (x_1, x_3) \in \Gamma^{(f,l)}, \quad l = 1, \ldots, J^{(f)},$$

$$\left(\boldsymbol{\sigma}(\mathbf{u}^{(l)})\mathbf{n}_{l,l+1} \cdot \mathbf{n}_{l,l+1}, \boldsymbol{\sigma}(\mathbf{u}^{(l)})\mathbf{n}_{l,l+1} \cdot \mathbf{m}_{l,l+1}\right)^{\top} \mathbf{B}^{(l)}(\omega) = ([\mathbf{u}] \cdot \mathbf{n}_{l,l+1}, [\mathbf{u}] \cdot \mathbf{m}_{l,l+1})^{\top}, \quad (x_1, x_3) \in \Gamma^{(f,l)}, \quad l = 1, \ldots, J^{(f)}, \tag{14}$$

where $\top$ indicates the transpose, $[\mathbf{u}]$ denotes the jump at $\Gamma^{(f,l)}$ of displacement vector $\mathbf{u}$, i.e.

$$[\mathbf{u}] = (\mathbf{u}^{(l)} - \mathbf{u}^{(l+1)})|_{\Gamma^{(f,l)}}$$

and

$$\mathbf{B}^{(l)}(\omega) = L \begin{pmatrix} Z_N^{(l)} & 0 \\ 0 & Z_T^{(l)} \end{pmatrix} \tag{15}$$

where $Z_N^{(l)}$ and $Z_T^{(l)}$ have the form (8), with $Z_V^{(l)} = Z_H^{(l)} = Z_T^{(l)}$.

The FE variational formulation is explained in detail in Santos *et al.* (2011, 2012), where *a priori* error estimates which are optimal for the regularity of the solution are given. The error is of the order of h in the L^2-norm and of the order of $\sqrt{h}$ both in the interior energy norm and in the L^2 norm on the set of fractures, where h is the size of the elements. The results on the existence and uniqueness of the solution of the continuous and discrete problems presented in that references apply to the cases analyzed here. The FE algorithms were implemented and validated in Fortran language, and were used to perform the numerical experiments presented in the next section.

4.2 Numerical experiments

The sample is subjected to time-harmonic compressions $\Delta P \exp(i\omega t)$, where P denotes pressure, and time-harmonic tangential forces $\Delta G \exp(i\omega t)$, where G is the shear stress (see Fig. 1). (Δ denotes a variation of the field variable). In the following we establish the boundary conditions to be used at the sides of the sample to obtain the stiffness components. Then, we solve eq. (13) with those conditions together with equations (14) at the interior of the grid (fracture interfaces).

(i) p_{33}: The boundary conditions are

$$[\boldsymbol{\sigma}(\mathbf{u}) \cdot \mathbf{n}] \cdot \mathbf{n} = -\Delta P, (x_1, x_3) \in \Gamma^T,$$

$$[\boldsymbol{\sigma}(\mathbf{u}) \cdot \mathbf{n}] \cdot \mathbf{m} = 0, \quad (x_1, x_3) \in \Gamma, \tag{16}$$

$$\mathbf{u} \cdot \mathbf{n} = 0, \quad (x_1, x_3) \in \Gamma^L \cup \Gamma^R \cup \Gamma^B.$$

In this experiment $e_{11} = e_{22} = 0$ and from the stress–strain relations (11) this experiment determines p_{33} as follows. Denoting by V the original volume of the sample and by $\Delta V(\omega)$ its (complex) oscillatory volume change, we note that

$$\frac{\Delta V(\omega)}{V} = -\frac{\Delta P}{p_{33}(\omega)}, \tag{17}$$

valid in the quasistatic case. After solving eqs (12) and (13) with the boundary conditions (16), the vertical displacements $u_3(x_1, \mathcal{L}, \omega)$ on Γ^T allow us to obtain an average vertical displacement $u_3^T(\omega)$ at the boundary Γ^T. Then, for each frequency ω, the volume change produced by the compressibility test can be approximated by $\Delta V(\omega) \approx \mathcal{L}u_3^T(\omega)$, which enable us to compute $p_{33}(\omega)$ by using the relation (17).

(ii) p_{11}: The boundary conditions are:

$$[\boldsymbol{\sigma}(\mathbf{u}) \cdot \mathbf{n}] \cdot \mathbf{n} = -\Delta P, \quad (x_1, x_3) \in \Gamma^R,$$

$$[\boldsymbol{\sigma}(\mathbf{u}) \cdot \mathbf{n}] \cdot \mathbf{m} = 0, \quad (x_1, x_3) \in \Gamma, \tag{18}$$

$$\mathbf{u} \cdot \mathbf{n} = 0, \quad (x_1, x_3) \in \Gamma^L \cup \Gamma^B \cup \Gamma^T.$$

In this experiment, $e_{33} = e_{22} = 0$ and this experiment determines p_{11} in the same way indicated for p_{33}.

(iii) p_{55}: The boundary conditions are:

$$\boldsymbol{\sigma} \cdot \mathbf{m} = \mathbf{g}, \quad (x_1, x_3) \in \Gamma^T \cup \Gamma^L \cup \Gamma^R,$$

$$\mathbf{u} = 0, \quad (x_1, x_3) \in \Gamma^B, \tag{19}$$
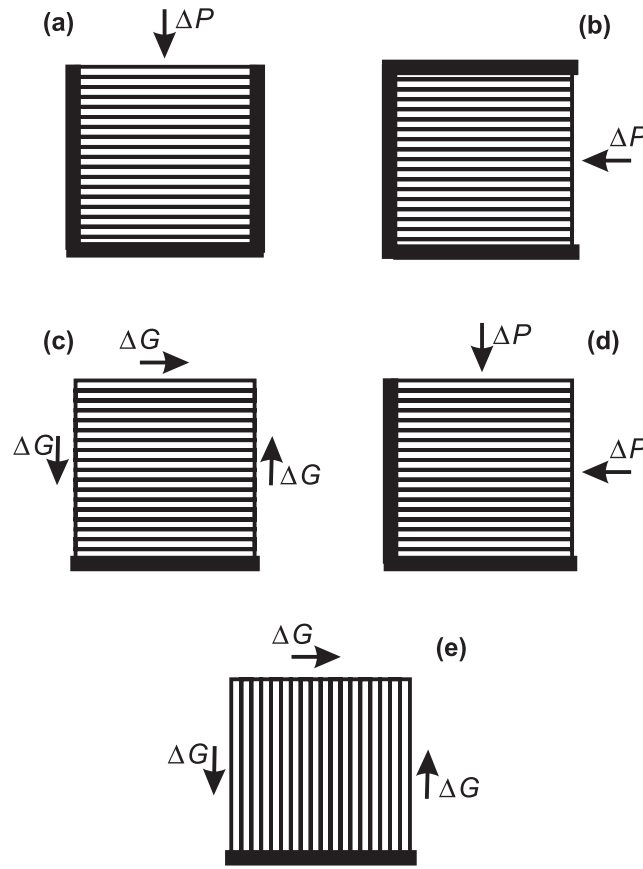
Figure 1. Oscillatory tests performed to obtain p_{33} (a), p_{11} (b), p_{55} (c), p_{13} (d) and p_{66} (e). The orientation of the layers and the directions of the applied stresses are indicated. The thick black lines at the edges indicate rigid boundary conditions (zero displacements).

where

$$\mathbf{g} = \begin{cases} (0, \Delta G), & (x_1, x_3) \in \Gamma^R, \\ (0, -\Delta G), & (x_1, x_3) \in \Gamma^L, \\ (\Delta G, 0), & (x_1, x_3) \in \Gamma^T. \end{cases}$$

The change in shape of the rock sample allow us to compute $p_{55}(\omega)$ by using the relation

$$\tan[\vartheta(\omega)] = \frac{\Delta G}{p_{55}(\omega)}, \tag{20}$$

where $\vartheta(\omega)$ is the angle between the original positions of the lateral boundaries and the location after applying the shear stresses.

The horizontal displacements $u_1(x_1, \mathcal{L}, \omega)$ at the top boundary Γ^T are used to obtain, for each frequency, an average horizontal displacement $u_1^T(\omega)$ at the boundary Γ^T. This average value allows us to approximate the change in shape suffered by the sample, given by $\tan[\vartheta(\omega)] \approx u_1^T(\omega)/\mathcal{L}$, which from eq. (20) yields $p_{55}(\omega)$.

(iv) p_{66}: Since this stiffness is associated with shear waves travelling in the (x_1, x_2)-plane, we take the layered sample, rotate it $90°$ and apply the shear test as indicated for p_{55}.

(v) p_{13}: The boundary conditions are

$$[\boldsymbol{\sigma}(\mathbf{u}) \cdot \mathbf{n}] \cdot \mathbf{n} = -\Delta P, \quad (x_1, x_3) \in \Gamma^R \cup \Gamma^T,$$

$$[\boldsymbol{\sigma}(\mathbf{u}) \cdot \mathbf{n}] \cdot \mathbf{m} = 0, \quad (x_1, x_3) \in \Gamma, \tag{21}$$

$$\mathbf{u} \cdot \mathbf{n} = 0, \quad (x_1, x_3) \in \Gamma^L \cup \Gamma^B.$$

Thus, in this experiment $e_{22} = 0$, and from the stress–strain relations (11) we obtain

$$\tau_{11} = p_{11}e_{11} + p_{13}e_{33},$$
$$\tau_{33} = p_{13}e_{11} + p_{33}e_{33}, \tag{22}$$

where e_{11} and e_{33} are the (macroscopic) strain components at the right lateral side and top side of the sample, respectively. Then from eq. (22) and using $\tau_{11} = \tau_{33} = -\Delta P$ [c.f. eq. (21)], we obtain

$$p_{13}(\omega) = \frac{p_{11}e_{11} - p_{33}e_{33}}{e_{11} - e_{33}}. \tag{23}$$

5 EXAMPLES

To verify that the FE implementation of the fractured medium is correct, we consider the data provided by the laboratory experiments of Chichinina *et al.* (2009). They consider an isotropic background medium defined by $c_{12} = 10$ GPa, $c_{55} = 3.9$ GPa ($c_{11} = 17.8$ GPa) and $\rho = 2300$ kg m^{-3}. Using their notation, they report $\Delta N = 1 - c_N = (0.28, -0.134)$ and $\Delta T = 1 - c_T = (0.15, -0.087)$ for a wet (oil-saturated) sample. Since

$$Z_N = \frac{1}{c_{11}} \left(\frac{1}{\Delta N} - 1 \right)^{-1} \quad \text{and} \quad Z_T = \frac{1}{c_{55}} \left(\frac{1}{\Delta T} - 1 \right)^{-1},$$

we obtain $Z_N^{-1} = (34, 24.7)$ GPa and $Z_T^{-1} = (15.5, 11.3)$ GPa. Similarly, we obtain the values for the dry sample: $Z_N^{-1} = (9.6, 4.8)$ GPa and $Z_T^{-1} = (3.1, 0.12)$ GPa. The frequency of the signal is $f_0 = 100$ kHz and the distance between fractures is $L = 1$ cm. Rewriting eq. (8) at the frequency f_0 as $Z_q^{-1} = \kappa_q + 2\pi i f_0 \eta_q, \ q = N, T$, we obtain

$$\kappa_q = \text{Re} \left(\frac{1}{Z_q} \right) \qquad \eta_q = \frac{1}{2\pi f_0} \text{Im} \left(\frac{1}{Z_q} \right). \tag{24}$$

Now, we set

$$Z_q = \frac{1}{\kappa_q + i\omega\eta_q}. \tag{25}$$

The following simulations have $L = 1$ cm, a grid spacing $dz = 0.5$ cm and $f_0 = 25$ Hz. To obtain p_{11}, p_{13} and p_{33}, we consider 29 equally spaced fractures and a FE mesh size of 60×60. On the other hand, p_{55} and p_{66} are obtained with 14 fractures and a mesh size of 30×30 grid points. The calculation of p_{66} requires an alternative treatment due to the fact that the sample is finite along the fracture planes which do
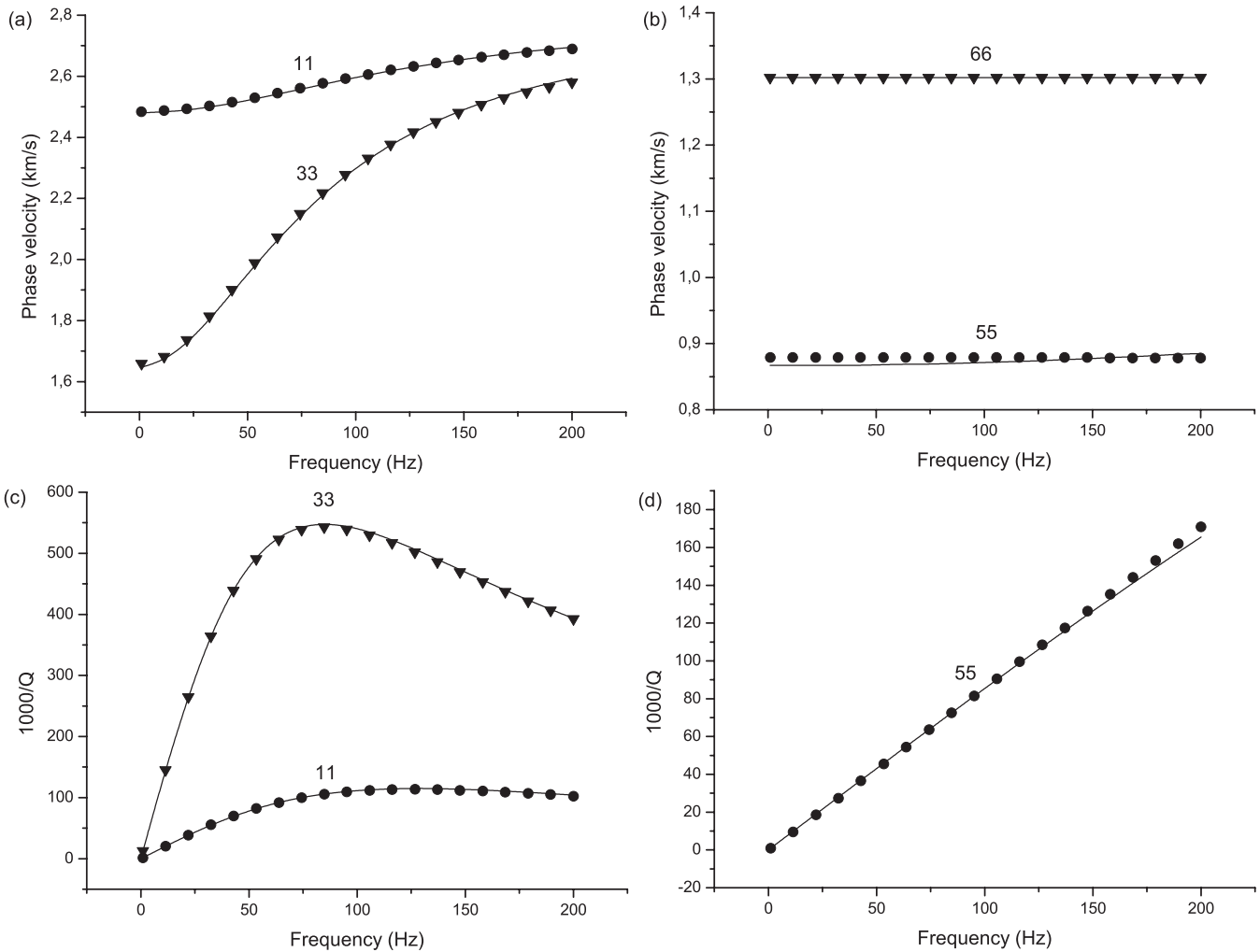

Figure 2. Phase velocities (a and b) and dissipation factors (c and d) as function of frequency corresponding to dry fractures. '11' and '66' refer to qP- and SH-waves travelling along the fracture plane and '33' refers to qP-waves travelling perpendicular the fracture plane, respectively, while '55' corresponds to the qS waves along and perpendicular to the fracture planes and to SH waves perpendicular to the fracture planes. The solid lines and symbols indicate the theoretical and numerical values, respectively.
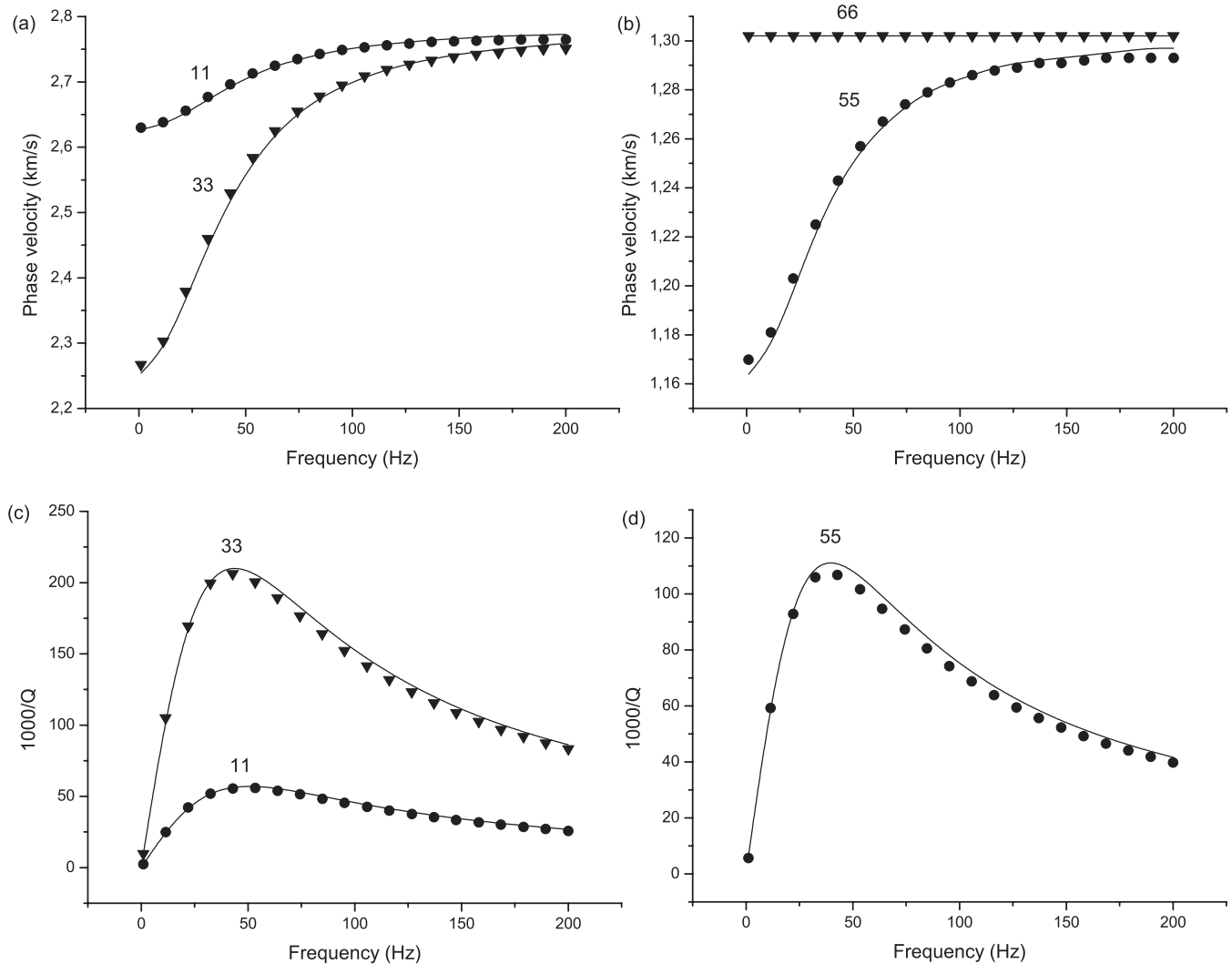
Figure 3. Phase velocities (a and b) and dissipation factors (c and d) as function of frequency corresponding to wet fractures. The solid lines and symbols indicate the theoretical and numerical values, respectively (see caption of Fig. 2).

not remain parallel after the deformation. In this case, we set to zero the displacement perpendicular to those planes. This constraint has no effect on the calculation since this component is uncoupled from the motion related to p_{66}.

The compliances Z_N and Z_T have the experimental values obtained above, but now the model has been scaled to seismic frequencies, i.e. $Z_N^{-1} = [34 + \mathrm{i}(f/f_0)\,24.7]$ GPa and $Z_T^{-1} = [15.5 + \mathrm{i}(f/f_0)\,11.3]$ GPa for the wet rock, and $Z_N^{-1} = [9.6 + \mathrm{i}(f/f_0)\,4.8]$ GPa and $Z_T^{-1} = [3.1 + \mathrm{i}(f/f_0)\,0.12]$ GPa for the dry rock. Actually, the determination of reliable fracture parameters requires measurements at the seismic range.

Figs 2 and 3 show the phase velocities and dissipation factors of the three wave modes along principal axes of the equivalent medium. The solid lines and symbols indicate the theoretical and numerical values, respectively. The dissipation factor associated to the '66' component is zero since $p_{66} = c_{55}$ is real (see eq. 9). The velocity dispersion of the qP wave is more pronounced in the dry case than in the wet case, while the opposite occurs for the qS wave. In both cases, the waves travel faster and attenuation is weaker for propagation along the fracture plane.

Fig. 4 shows the energy velocities and dissipations factors as a function of the angle (energy and phase angles, respectively). The frequency is 53 Hz. The dry case shows more anisotropy and attenuation. The qP wave is strongly attenuated along the direction perpendicular to the fractures ($\theta = 0°$), while the qS wave has higher loss at approximately $50°$ in the dry case but shows the opposite behaviour in the wet case, where attenuation has a minimum at about $40°$. The SH wave has no loss in the direction parallel to the fractures since p_{66} is real.

These features are in qualitative agreement with the experimental data (phase velocity and dissipation factor) reported by Chichinina *et al.* (2009) in their Figs 2 and 3, providing a confirmation of the linear-slip theory. Strong shear-wave splitting is observed at all frequencies in the dry case along the fracture plane, while P-wave anisotropy occurs at low frequencies. *Q* anisotropy is more pronounced than velocity anisotropy, and stronger attenuation characterizes the fluid-filled fractures. Moreover, as can be seen in the wet case, velocity anisotropy is small but attenuation anisotropy can be high. It is evident the strong frequency dependence of the wave properties. For instance, the stiffness
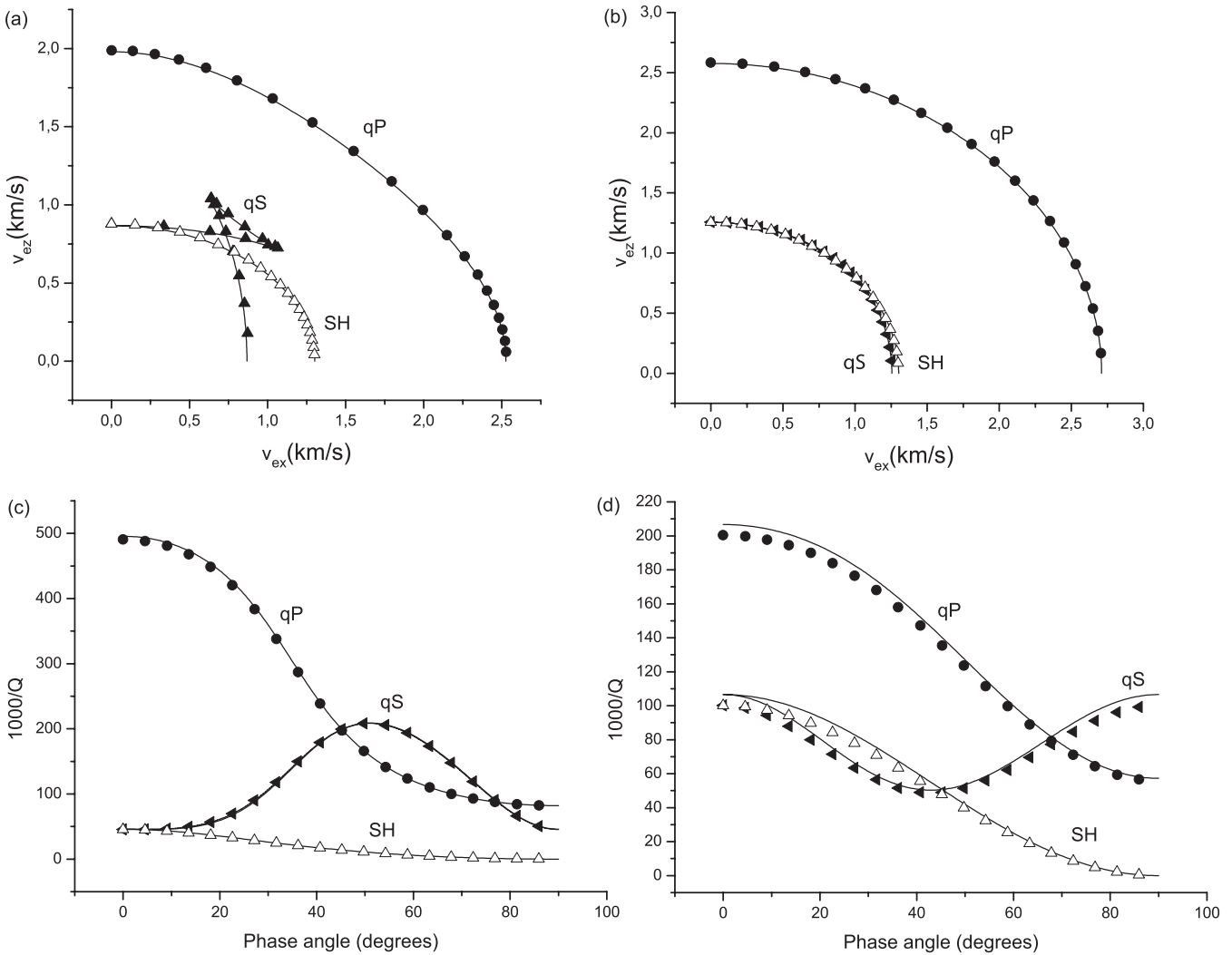
Figure 4. Energy velocity (a and b) and dissipation factors (c and d) as a function of angle for dry (a and c) and wet (b and d) fractures. The frequency is 53 Hz. The solid lines and symbols indicate the theoretical and numerical values, respectively.

related to the '33' direction is $p_{33} = c_{11}(\kappa_N + i\omega\eta_N)/(\kappa_N + i\omega\eta_N + c_{11})$, with $p_{33} = c_{11}/(1 + c_{11}/\kappa_N)$ at $\omega = 0$ and $p_{33} = c_{11}$ at $\omega = \infty$, both lossless limits. Then, the factor $\sqrt{1 + c_{11}/\kappa_N}$ quantifies the amount of velocity dispersion. There is no dispersion and loss for $\kappa_N = \infty$, corresponding to a welded interface.

Next we consider non-equispaced fractures and compare numerical and analytical solutions. According to Schoenberg (1983), the requirement of equally spaced fractures can be relaxed as long as Z_N and Z_T are the same for all the fractures. Using our notation, he states: 'It should be noted here that we can relax the requirement that we have equally spaced identical cracks. As the slip is manifest in the two dimensionless compliances $c_{55}Z_T$ and $c_{55}Z_N$, a homogeneous material with irregularly spaced parallel slip interfaces behaves identically as long as $Z_T = Z_2/L$ and $Z_N = Z_1/L$ are the same (where Z_2 is the total tangential slip of all the cracks in distance L due to unit shear stress, and Z_1 is the total normal slip due to unit normal stress). Thus a rock with arbitrary closely spaced parallel linear slip interfaces can be modelled as a homogeneous transverse isotropic solid as long as the average slip per distance normal to the system of cracks is independent of x_3'.

We consider a periodic system where the vertical location of the fractures is given by the array of grid points [(4, 6), (10, 12), (16, 18), (22, 24), . . .] dz, where the parentheses indicate a pair separated by a distance $2dz$. For each pair is $Z_1 = (a, b)LZ_N$ and $Z_2 = (c, d)LZ_T$, with $a + b = c + d = 1$, such that the total normal and tangential displacement discontinuities per unit stress in one period are LZ_N and LZ_T, respectively. For instance, eq. (2) for each fracture pair and unit stress is

$$[u_z] = [u_z](\text{fracture 1}) + [u_z](\text{fracture 2}) = aLZ_N + bLZ_N = LZ_N,$$

$$[u_x] = [u_x](\text{fracture 1}) + [u_x](\text{fracture 2}) = cLZ_T + dLZ_T = LZ_T. \tag{26}$$

We consider the wet case, a 100×100 mesh of 25 cm side length and 32 fractures to compute p_{11} and p_{33} and a 64×64 mesh of 16 cm side length and 20 fractures to compute p_{55}. We take $dz = 0.25$ cm (the period is $L = 1.5$ cm) and combinations of sets (a, b) and (c, d) equal to $(0.5, 0.5)$, $(1/3, 2/3)$ and $(0.9,0.1)$. The results indicate that the numerical and analytical solutions coincide and are not shown because they
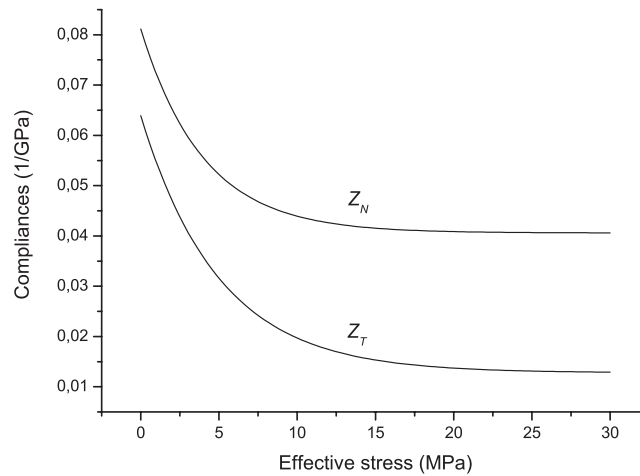
Figure 5. Real part of the compliances as a function of effective stress.

are similar to those of Fig. 3. The case (0.5, 0.5) corresponds to considering an effective L being the average fracture spacing (0.75 cm), as indicated in Grechka *et al.* (2003).

Next, we use the FE simulations in cases for which no analytical solutions are available. To obtain a set of stiffness coefficients p_{IJ} representative of the medium it is required the condition of stationarity. That is, in a given length of medium much smaller than the wavelength, the properties of the background material and fracture stiffnesses are constant on average (periodicity is not required).

Let us now consider fractures at varying pore fluid pressure. Daley *et al.* (2006) suggest that a reasonable assumption is to take high values of fracture compliance at low normal effective stress. Then, the fracture compliances approach low values asymptotically as normal stress increases. They propose

$$Z_q = Z_{q\infty} + (Z_{q0} - Z_{q\infty})\exp(-\sigma/\tau_q), \tag{27}$$

where Z_{q0}, $Z_{q\infty}$ and τ_q are constants, and $\sigma = p_c - p$ is the effective normal stress, where p_c is the confining pressure and p is the pore pressure. Following Daley *et al.* (2006) we consider $\Delta N0 = (0.2, -0.02)$ and $\Delta T0 = (0.6, -0.06)$, where the imaginary part here has been chosen as one tenth of the real part, with $\tau_N = 4$ MPa and $\tau_T = 5$ MPa. Moreover, $Z_{N0} = 2Z_{N\infty}$ and $Z_{T0} = 5Z_{T\infty}$. For a constant confining pressure $p_c = 30$ MPa, Fig. 5 shows the real parts of the compliances as a function of the effective stress.

Let us consider two pore pressures 5 and 28 MPa, normal and overpressure values, respectively. We obtain from eq. (27)

$$p = 5 \text{ MPa}: \quad Z_N^{-1} = (23.1 + 5.9i) \text{ GPa}, \quad Z_T^{-1} = (75 + 9.4i) \text{ GPa},$$

$$p = 28 \text{ MPa}: Z_N^{-1} = (14.4 + 3.6i) \text{ GPa}, \quad Z_T^{-1} = (21 + 2.6i) \text{ GPa}, \tag{28}$$

such that these values correspond to $f = 25$ Hz since we have taken $f_0 = 25$ Hz. We then consider a set of equispaced fractures with $L = 1$ cm and 80 per cent binary fractal variations of the compliances Z_N and Z_T around the mean values given by eq. (28), where binary means that these compliances take only two values, ± 80 per cent around their mean values. The correlation length is 0.7 (in a scale of 10) and the fractal dimension is 2.2. We model fractal variations by using a von Kármán autocovariance probability function (von Kármán 1948). The background medium is that defined above and we have used the same mesh parameters as in Figs 2 and 3. Fig. 6 compares the energy velocity (a and b) and dissipation factors (c) for the normal and overpressure cases. As expected, increasing pore pressure implies lower velocity and more anisotropy. This effect can clearly be seen in the wavefronts. On the other hand, attenuation is stronger in the overpressured case and along the vertical direction.

Finally, we consider the problem solved to obtain Fig. 2 (the dry case) with 50 per cent binary fractal variations of the background Lamé constants λ and μ, as shown in Figs 7(a) and (b). The correlation length is 0.7 (in a scale of 10), the fractal dimension is 2.2 and we have used the same mesh parameters as in Figs 2 and 3. Figs 7(c) and (d) show the phase velocity and dissipation factor as a function of frequency. The velocities in the fractal case are lower than those obtained with the mean values, while only the dissipation factor of the qP wave travelling along the direction perpendicular to the fractures is affected, showing lower values in the fractal case.

6 CONCLUSIONS

Schoenberg's theory predicts that an homogeneous background containing a set of horizontal parallel fractures behaves like a transversely isotropic medium at long wavelengths. We presented a collection of novel numerical quasi-static harmonic experiments to test and validate the theory. The proposed experiments are based on a finite-element solution of the equation of motion in the space-frequency domain to simulate compressibility and shear tests. The fracture behaviour is modelled as discontinuities of the displacements and velocity fields and continuity of stresses at the fracture interfaces, i.e. the fractures are represented as a set of internal boundaries in the finite-element domain. The phase, energy and dissipation factors as a function of the propagation and ray (energy) angle are obtained for homogeneous viscoelastic
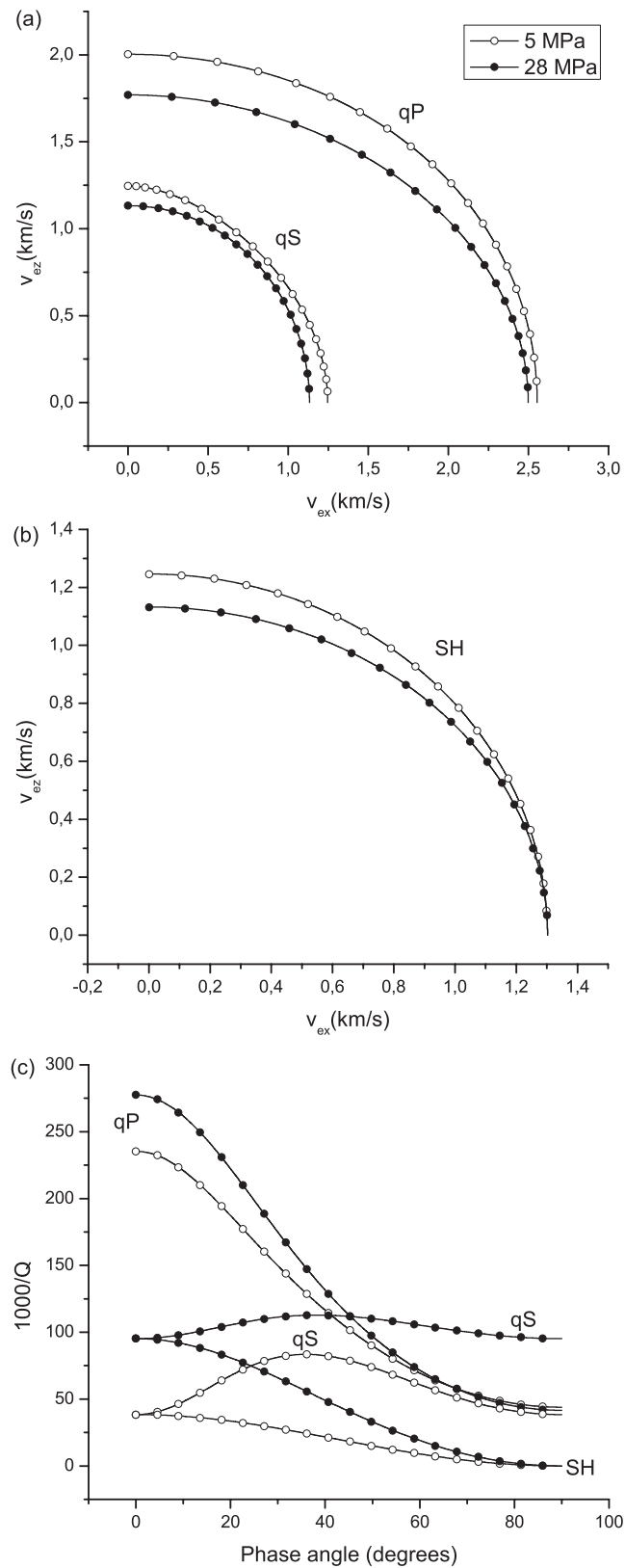
Figure 6. Energy velocity (a and b) and dissipation factor (c) versus angle for the normal (open circles) and overpressure (full circles) cases. Fractal variations of the fracture stiffnesses are modelled. The frequency is 25 Hz.
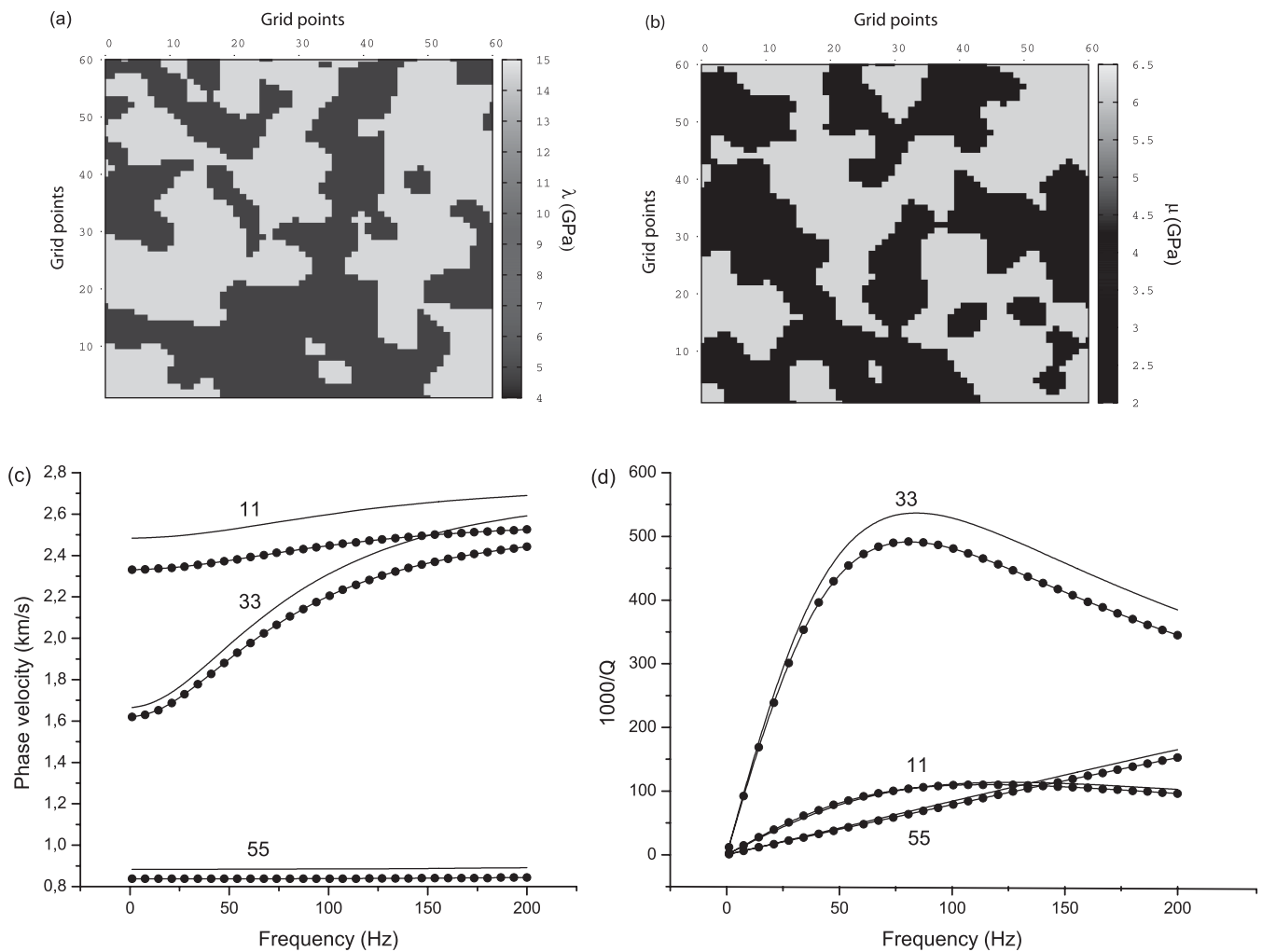
Figure 7. Fractal variations of the background Lamé stiffnesses (a and b), phase velocity (c) and dissipation factor (d) as a function of frequency. The solid lines are the FE results computed with the mean values and the solid lines with symbols correspond to the fractal case.

plane waves (wavenumber and attenuation directions coincide). Attenuation is solely due to fracture viscosity while the background medium is lossless.

For periodic, non-equispaced fractures the numerical results show a good match with the analytical solution. A medium with arbitrary closely spaced parallel and horizontal fractures can be modelled as an effective transverse isotropic solid as long as the average displacement per distance normal to the system of fractures is independent of the vertical coordinate. Then, we apply the method to cases where there is no analytical solution, such as random variations of the fracture stiffnesses at different pore pressures and fractal variations of the background elastic properties. In particular, it is shown that attenuation can be an indicator of overpressure with higher values at high pore pressures.

The model can be important in determining the orientation of fractures in the reservoir and the overlying cap rock. This plays an important role in the oil industry during production, and other applications, such as CO_2 injection and monitoring.

ACKNOWLEDGMENTS

REFERENCES

Ben-Menahem, A. & Singh, S.J., 1981. *Seismic Waves and Sources,* Springer-Verlag, New York, NY.

Carcione, J.M., 1992. Anisotropic Q and velocity dispersion of finely layered media, *Geophys. Prospect.,* **40,** 761–783.

Carcione, J.M., 1996. Elastodynamics of a non-ideal interface: application to crack and fracture scattering, *J. geophys. Res.,* **101,** 28177–28188.

Carcione, J.M., 1998. Scattering of elastic waves by a plane crack of finite width in a transversely isotropic medium, *Int. J. Numer. Anal. Methods Geomech.,* **22,** 263–275

Carcione, J.M., 2007. *Wave fields in real media: wave propagation in anisotropic, anelastic, porous and electromagnetic media,* Handbook of Geophysical Exploration, Vol. 38, 2nd edn, Elsevier, Amsterdam.

Carcione, J.M., Santos, J.E. & Picotti, S., 2011. Anisotropic poroelasticity and wave-induced fluid flow. Harmonic finite-element simulations, *Geophys. J. Int.,* **186,** 1245–1254.

Carcione, J.M., Santos, J.E. & Picotti, S., 2012. Fracture-induced anisotropic attenuation, *Rock Mech. Rock Eng.,* **45,** 929–942, doi:10.1007/s00603-012-0237-y.

Chichinina, T.I., Obolentseva, I.R. & Ronquillo-Jarillo, G., 2009. Anisotropy of seismic attenuation in fractured media: theory and ultrasonic experiment, *Transport Porous Media,* **79,** 1–14.

Coates, R.T. & Schoenberg, M., 1995. Finite-difference modelling of faults and fractures, *Geophysics,* **60,** 1514–1526.

Daley, T.M., Schoenberg, M.A., Rutqvist, J. & Nihei, K.T., 2006. Fractured reservoirs: an analysis of coupled elastodynamic and permeability changes from pore-pressure variation, *Geophysics,* **71,** O33–O41.

Daub, E.G. & Carlson, J.M., 2010. Friction, fracture, and earthquakes, *Ann. Rev. Condensed Matter Phy.,* **1,** 397–418.

De Basabe, J.D., Sen, M.K. & Wheeler, M.F., 2011. Seismic wave propagation in fractured media: a discontinuous Galerkin approach, SEG Expanded Abstr., **30,** 2920, doi:10.1190/1.3627801.

Gray, F.D. & Head, K., 2000. Fracture detection in the Manderson Field: a 3-D AVAZ case history, 70th Ann. Int. Mtg., *Soc. Expl. Geophys.,* 1413–1416.

Grechka, V.A., Bakulin, A. & Tsvankin, I., 2003. Seismic characterization of vertical fractures described as general linear-slip interfaces, *Geophys. Prospect.,* **51,** 117–130.

Liu, E., Hudson, J.A. & Pointer, T., 2000. Equivalent medium representation of fractured rock, *J. geophys. Res.,* **105,** 2981–3000.

Nelson, R.A., 2001. *Geologic Analysis of Naturally Fractured Reservoirs,* 2nd edn, Gulf Publishing Co, Woburn, MA.

Picotti, S., Carcione, J.M., Santos, J.E. & Gei, D., 2010. Q-anisotropy in finely layered media, *Geophys. Res. Lett.,* **37,** L06302, doi:10.1029/2009GL042046.

Picotti, S., Carcione, J.M. & Santos, J.E., 2012. Oscillatory numerical experiments in finely layered anisotropic viscoelastic media, *Computers Geosci.,* **43,** 83–89.

Pyrak-Nolte, L.J., Myer, L.R. & Cook, N.G.W., 1990. Transmission of seismic waves across single natural fractures, *J. geophys. Res.,* **95,** 8617–8638.

Santos, J.E., Carcione, J.M. & Picotti, S., 2011. Viscoelastic-stiffness tensor of anisotropic media from oscillatory numerical experiments, *Computer Methods Appl. Mech. Eng.,* **200,** 896–904.

Santos, J.E., Picotti, S. & Carcione, J.M., 2012. Evaluation of the stiffness tensor of a fractured medium with harmonic experiments, *Computer Methods Appl. Mech. Eng.,* **247–248,** 130–145.

Santos, J.E., Rubino, J.G. & Ravazzoli, C.L., 2009. A numerical upscaling procedure to estimate effective plane wave and shear moduli in heterogeneous fluid-saturated poroelastic media, *Computer Methods Appl. Mech. Eng.,* **198,** 2067–2077.

Schoenberg, M., 1980. Elastic wave behavior across linear slip interfaces, *J. acoust. Soc. Am.,* **68,** 1516–1521.

Schoenberg, M., 1983. Reflection of elastic waves from periodically stratified media with interfacial slip, *Geophys. Prospect.,* **31,** 265–292.

Schoenberg, M., Dean, S. & Sayers, C., 1999. Azimuth-dependent tuning of seismic waves reflected from fractured reservoirs, *Geophysics,* **64,** 1160–1171.

Steen, O., Sverdrup, E. & Hanssen, T.H., 1998. Predicting the distribution of small faults in a hydrocarbon reservoir by combining outcrop, seismic and well data, *Geol. Soc. Lond. Special Publ.,* **147,** 27–50, doi:10.1144/GSL.SP.1998.147.01.03.

von Kármán, T., 1948. Progress in the statistical theory of turbulence, *J. Marine Res.,* **7,** 252–264.

Xu, T.F. & Pruess, K., 2001. Modeling multiphase non-isothermal fluid flow and reactive geochemical transport in variably saturated fractured rocks: 1. Methodology, *Am. J. Sci.,* **301,** 16–33.

Zhang, J., 2005. Elastic wave modeling in fractured media with an explicit approach, *Geophysics,* **70,** T75–T85.

Zhang, J. & Gao, H., 2009. Elastic wave modelling in 3-D fractured media: an explicit approach, *Geophys. J. Int.,* **177,** 1233–1241.

APPENDIX: WAVE VELOCITIES AND QUALITY FACTORS

The complex velocities are required to calculate wave velocities and quality factors of the fractured medium. They are given by

$$v_{qP} = (2\rho)^{-1/2}\sqrt{p_{11}l_1^2 + p_{33}l_3^2 + p_{55} + A},$$

$$v_{qS} = (2\rho)^{-1/2}\sqrt{p_{11}l_1^2 + p_{33}l_3^2 + p_{55} - A},$$

$$v_{SH} = \rho^{-1/2}\sqrt{p_{66}l_1^2 + p_{55}l_3^2},$$

$$A = \sqrt{[(p_{11} - p_{55})l_1^2 + (p_{55} - p_{33})l_3^2]^2 + 4[(p_{13} + p_{55})l_1 l_3]^2},$$

(A1)

(Carcione 2007), where $l_1 = \sin\theta$ and $l_3 = \cos\theta$ are the directions cosines, θ is the propagation angle between the wavenumber vector and the symmetry axis, and the three velocities correspond to the qP, qS and SH waves, respectively. The phase velocity is given by

$$v_p = \left[\text{Re}\left(\frac{1}{v}\right)\right]^{-1},$$

(A2)

where v represents either v_{qP}, v_{qSV} or v_{SH}. The energy-velocity vector of the qP and qS waves is given by

$$\frac{\mathbf{v}_e}{v_p} = (l_1 + l_3\cot\psi)^{-1}\hat{\mathbf{e}}_1 + (l_1\tan\psi + l_3)^{-1}\hat{\mathbf{e}}_3,$$

(A3)

(Carcione 2007), where

$$\tan\psi = \frac{\text{Re}(\beta^* X + \xi^* W)}{\text{Re}(\beta^* W + \xi^* Z)},$$

(A4)

defines the angle between the energy-velocity vector and the *z*-axis,

$$\beta = \sqrt{A \pm B},$$

$$\xi = \pm\text{pv}\sqrt{A \mp B},$$

(A5)

$$B = p_{11}l_1^2 - p_{33}l_3^2 + p_{55}\cos 2\theta,$$

where the upper and lower signs correspond to the qP and qS waves, respectively. Moreover,

$$W = p_{55}(\xi l_1 + \beta l_3),$$
$$X = \beta p_{11} l_1 + \xi p_{13} l_3, \tag{A6}$$
$$Z = \beta p_{13} l_1 + \xi p_{33} l_3,$$

(Carcione 2007), where 'pv' denotes the principal value, which has to be chosen according to established criteria.

On the other hand, the energy velocity of the SH wave is

$$\mathbf{v}_e = \frac{v_p}{\rho \mathrm{Re}(v)} \left[l_1 \mathrm{Re}\left(\frac{p_{66}}{v}\right) \hat{\mathbf{e}}_1 + l_3 \mathrm{Re}\left(\frac{p_{55}}{v}\right) \hat{\mathbf{e}}_3 \right]. \tag{A7}$$

Finally, the quality factor is given by

$$Q = \frac{\mathrm{Re}(v^2)}{\mathrm{Im}(v^2)}. \tag{A8}$$